quantum reports

MDPI

Article

Distinguishing a Two-Step Quantum–Classical Threshold from Collapse Models

Raghu Kulkarni

SSMTheory Group, IDrive Inc., Calabasas, CA 91302, USA; raghu@idrive.com

Abstract

A model of the vacuum as a face-centered-cubic lattice predicts a two-step quantum–classical threshold, at 13.1 and 22.6 μg, from the hypothesis (P3) that a center-of-mass excitation stays coherently representable only while its reduced Compton wavelength is resolvable by the lattice. Collapse models also limit macroscopic coherence, so the two must be told apart by more than a scale. Taking P3 as a hypothesis, not a derived result, we derive discriminators from the model's postulates and compute the counterpart in Diósi–Penrose collapse and in continuous spontaneous localization (CSL). The thresholds depend on total mass alone, the same for every material, while both collapse models depend on density. Below 13.1 μg, the model predicts no intrinsic decoherence, where collapse takes 1 s for Diósi–Penrose and about a microsecond for CSL at its experimental bound, for 10^{-15} kg over 1 μm; this also separates the model from energy-driven reduction models, which dephase at every mass. The model predicts no measurable heating. Two consistency requirements follow: read as position localization, its rate scale would exceed the LISA Pathfinder bound by 66 orders of magnitude, and read as strong energy-basis dephasing it would destroy the phase of classical oscillations of macroscopic bodies. The Compton-scale correction does not alter the motion of microgram bodies. If the effective mass of a mechanical mode is the relevant mass, a mechanical cat state quoted at 16.2 μg bounds the irreversible coupling at 37 orders below its natural scale; in another common convention, that mode is below the threshold. A worked levitated-particle example, an outlook for near-future data, and a public script complete the analysis.

Keywords: quantum–classical threshold; Diósi–Penrose collapse; continuous spontaneous localization; macroscopic superposition; decoherence; lattice vacuum; Compton wavelength; mechanical cat states

1. Introduction

Where quantum mechanics stops applying to massive objects, if it stops at all, is an open experimental question. Collapse models answer it with a new physical process. The best known, due to Diósi and Penrose [1–3] (DP), ties the collapse of a spatial superposition to the gravitational self-energy of the difference between its branches and predicts a collapse time $\tau_{\mathrm{DP}} = \hbar/E_G$. Continuous spontaneous localization [4,5] (CSL) instead adds a universal stochastic localization with a rate λ and a length r_C, both constrained by experiment; at the standard r_C, its originally proposed strength is now excluded [6]. A large body of work tests these models, interferometrically and through the heating and radiation they cause [5,7–11]. A further class, energy-driven stochastic reduction [12–15], dephases in the energy basis and conserves energy.

Check for updates

Received: 1 October 2026
Revised: 29 October 2026
Accepted: 2 November 2026
Published: 4 November 2026

Copyright: © 2026 by the author. Licensee MDPI, Basel, Switzerland. This article is an open access article distributed under the terms and conditions of the Creative Commons Attribution (CC BY) license.

A recent paper [16] proposed a different answer from a discrete model of the vacuum, a face-centered-cubic (FCC) lattice with Bell-pair bonds. It predicts two thresholds, at $m_{\text{soft}} = 13.1\,\mu\text{g}$ and $m_{\text{hard}} = 22.6\,\mu\text{g}$, in the exact ratio $\sqrt{3}$, from the hypothesis P3 stated in Section 3. That paper noted that the scale itself is not new, since DP also predicts a scale of order the Planck mass. It distinguished the two models by the two-step structure and by the absence of any dependence on the separation Δx between branches. A Heisenberg cut at the Planck mass, from the same comparison of the reduced Compton wavelength with the Planck length, has also been proposed on independent grounds [17], with a self-decoherence model in which the internal vibrations of such bodies stay quantum [18]. Most of the tests developed here apply to a threshold of that kind as well.

Both distinctions require reaching the 13–23 μg window, which is beyond present superposition experiments. This paper asks what else the same postulates predict, closer to present experiments, and what existing data already imply.

Main results. (i) The thresholds depend on total mass alone, so two bodies of equal mass and different density share them; DP and CSL do not (Section 5). (ii) Below m_{soft}, the model predicts no intrinsic decoherence at any separation or time, where DP, CSL, and energy-driven reduction all predict finite rates (Section 6). (iii) The model produces no measurable heating or radiation. This yields two consistency requirements on the model itself. Its loss of coherence above threshold can be neither position localization at the lattice scale, excluded by LISA Pathfinder by 66 orders of magnitude, nor strong energy-basis dephasing, excluded by the phase stability of macroscopic oscillators (Section 7). (iv) The Compton-scale correction that sets the thresholds leaves the motion of microgram bodies unchanged, so existing precision oscillators do not constrain it (Section 3). (v) An existing mechanical cat state bounds the irreversible coupling in the window, conditionally on the mass assigned to an acoustic mode (Section 8). (vi) Phonon-number statistics and a Hahn echo separate the remaining channel types (Sections 7 and 9).

What is new? Existing tests of collapse models bound a rate that grows with mass and separation. The lattice model instead fixes a mass scale with no adjustable parameter, from one calibration of the lattice spacing, and predicts an exact null below it. The material ratio of Section 5, the comparison with energy-driven reduction, the two consistency requirements, and the conditional bound from an existing experiment are, to our knowledge, new. Section 10 gives the margin that near-future data can reach.

Section 2 summarizes the framework for readers new to it. Each claim is labeled by status: *derived* from the stated postulates, *computed* from a stated formula, or *open*. A public script reproduces every number (Data Availability Statement). The framework's other ingredients are published in refereed work [16,19,20], except the vacuum code [21], which is a preprint; none of them has been tested independently, and the derivations here use only the postulates of Section 3.

2. The Selection–Stitch Model in Brief

2.1. The Vacuum Lattice

The Selection–Stitch Model (SSM) treats the vacuum as a discrete network instead of a continuum. Its nodes form a face-centered-cubic (FCC) lattice, the densest packing of equal spheres, in which every node has twelve nearest neighbors arranged as a cuboctahedron. Each bond is a maximally entangled pair of qubits, a Bell pair. In the series, this lattice arises from a growth process of in-plane "stitches" and rare out-of-plane "lifts" that crystallizes into FCC packing [19], and it carries a quantum error-correcting code, so the vacuum behaves as a protected quantum memory [21]. These results motivate the framework, but the derivations below use only the postulates stated in Section 3.

https://doi.org/10.3390/quantum8040117

2.2. Matter as Trapped Nodes

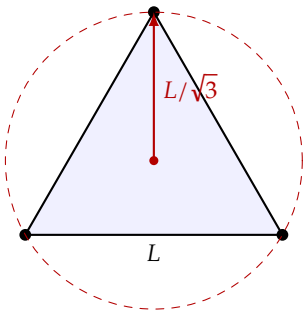
Matter, in this picture, is a defect of the vacuum: an extra node trapped in one of the lattice's tetrahedral voids, which cannot relax into the twelve-coordinated bulk and so persists as a localized object [19]. A defect moves by hopping between adjacent voids [20]. A macroscopic body is a large collection of such defects. The hypothesis P3 of Section 3 treats the center-of-mass motion of such a body, when it is in a superposition, as one collective excitation of the lattice, characterized by its total rest energy.

2.3. One Length Scale

The lattice has one length scale, the bond length L. It is fixed by a single calibration, matching the entanglement entropy of the code to the Bekenstein–Hawking area law, which gives $L = \sqrt{4 \ln 2}\, \ell_P \approx 1.665\, \ell_P$, about 2.7×10^{-35} m [16]. The entropy is the von Neumann entanglement entropy, and each stabilizer plaquette that the boundary cuts contributes $\ln 2$, the entropy of one Bell pair. The entanglement spectrum of a stabilizer state is flat, so every Rényi entropy has the same value, and the calibration does not depend on that choice. At wavelengths much longer than L, the lattice is invisible. Provided all low-energy modes share one propagation speed, low-energy physics is isotropic and Lorentz-invariant, with violations suppressed by $(E/E_P)^2$, about 10^{-56} at optical energies [16]. Ordinary quantum mechanics holds to extraordinary precision, except where the hypothesis below applies.

2.4. How a Threshold Arises

The lattice becomes relevant only when some scale associated with a body's center-of-mass motion approaches L. The SSM's hypothesis is that the relevant scale is the reduced Compton wavelength, which we write as $\ell_C = \hbar/(mc)$ to keep the symbol λ for the CSL rate. Unlike the size of a body, ℓ_C shrinks as the mass grows, and it equals L at $m = \hbar/(Lc) \approx 13\,\mu$g. The lattice scale is Planckian, but the mass at which ℓ_C reaches it is macroscopic. The two thresholds come from two lengths of the cuboctahedral geometry, the edge L and the circumradius $L/\sqrt{3}$ of a triangular face (Figure 1).



$\ell_C = L$: $m_{\text{soft}} = \hbar/(Lc)$

$\ell_C = L/\sqrt{3}$: $m_{\text{hard}} = \sqrt{3}\, m_{\text{soft}}$

Figure 1. A triangular face of the cuboctahedron formed by a node's twelve neighbors. The soft threshold is the mass whose reduced Compton wavelength equals the edge L, whereas the hard threshold is the mass whose reduced Compton wavelength equals the circumradius $L/\sqrt{3}$. Their ratio, $\sqrt{3}$, is fixed by the geometry alone.

Representability. We call a state of a collective excitation *representable* when the lattice can carry the phase structure set by its rest energy, $e^{-imc^2 t/\hbar}$, which oscillates at the Compton frequency $mc^2/\hbar$; the corresponding length is c divided by that frequency, ℓ_C. The lattice's own dispersion measures how well it does so: at wavenumber k, the correction to the continuum dispersion is of relative size $(kL)^2/6$, and at the Compton wavenumber $k_C = 1/\ell_C$, this equals $\delta(m) = \frac{1}{6}(m/m_{\text{soft}})^2$ [16]. Representability is good while this is small, degrades when $\ell_C = L$, and fails when ℓ_C reaches the shortest length the lattice can resolve, the circumradius $L/\sqrt{3}$.

2.5. Why the Compton Wavelength, and Why the Total Mass?

Three other lengths could seem more natural: the de Broglie wavelength, the width of the wave packet or the separation Δx between branches, and the Compton wavelengths of the constituents. The model's structure, not evidence, decides among them.

The width of the wave packet and the separation Δx describe a particular state, not the excitation, and they exceed L by many orders of magnitude; a threshold set by them would depend on Δx, which the model does not predict [16]. The Compton wavelengths of the constituents also exceed L by far. If representability were decided constituent by constituent, there would be no threshold at all and the model would reduce to standard quantum mechanics for every body.

The de Broglie wavelength h/p governs the wave behavior of center-of-mass motion, but it depends on the frame through the momentum. It also gives the wrong answer at both ends. For a slow microgram body, it is far longer than L, so the lattice would never matter. For a fast macroscopic body, it is shorter than L: a 1 kg body moving at 1 m/s has $pL/\hbar \approx 0.26$. If the lattice dispersion acted on the center-of-mass momentum of a composite body, its kinetic energy would be off by about 1%, and a car would lie beyond the edge of the Brillouin zone. This is the "soccer-ball problem" of models in which a Planck-scale deformation acts on the total momentum of a composite body [22,23]. The model avoids it because the lattice dispersion acts on the elementary excitations, the trapped nodes of Section 2, whose momenta are tiny: for a nucleon at 1 m/s, the correction is about 3×10^{-56}. The kinetic energy of a composite body is the sum of these, so its motion is unaffected.

P3 uses the total mass for a different question: whether the coherent collective state as a whole can be carried by the lattice. Its scale is set by the rest energy, which is the same in every frame, and ℓ_C is the frame-independent length associated with it. That a Planck-scale structure couples to the total mass of a coherent collective excitation, while the motion of the body follows its constituents, is the content of P3. It is not derived from P1 and P2, and every discriminator in this paper inherits its status as a hypothesis. Molecule interferometry beyond 25 kDa shows that the center-of-mass quantum mechanics of composite objects depends on their total mass [24]; it does not show that a Planck-scale structure couples to that mass.

Internal structure enters only through the rest energy. Two bodies of equal mass but different composition, density, or internal state have the same ℓ_C, and internal energy changes the rest mass of a room-temperature solid by about 3×10^{-12} of itself. P3 thus assigns the same threshold to every composite body of a given mass. This is what Section 5 tests.

3. The Threshold and Its Postulates

We restate only what the derivations use; Ref. [16] gives the full construction. The published model rests on three postulates: P1, the FCC network with Bell-pair bonds; P2, the calibration of L described in Section 2.3; and P3, Compton representability.

P3 (Compton representability). A center-of-mass excitation, characterized by its total rest energy mc^2, remains coherently representable on the lattice only while its reduced Compton wavelength $\ell_C = \hbar/(mc)$ is resolvable by the lattice geometry. P3 is a hypothesis (Section 2.5).

Representability first degrades when $\ell_C = L$ and fails when ℓ_C equals the circumradius $L/\sqrt{3}$ of a triangular face:

$$m_{\text{soft}} = \frac{\hbar}{Lc} = 13.07\,\mu\text{g}, \qquad m_{\text{hard}} = \sqrt{3}\, m_{\text{soft}} = 22.64\,\mu\text{g}. \tag{1}$$

The lattice correction is Hermitian. Its size, evaluated at the Compton wavenumber, is $\delta(m) = \frac{1}{6}(m/m_{\text{soft}})^2$, which grows from 1/6 at m_{soft} to 1/2 at m_{hard} [16].

What the two masses mean, and how they are decided. In theory, both follow from P3 and the single calibration of L. m_{soft} is the mass whose reduced Compton wavelength equals L, where representability first degrades; m_{hard} is the mass at which it equals the circumradius $L/\sqrt{3}$, where representability fails. Their ratio $\sqrt{3}$ is fixed by the geometry alone and does not depend on the calibration. They matter because they are the model's only scales for an intrinsic loss of coherence: below m_{soft}, none occurs, and above m_{hard}, the published model does not sustain coherence. The experiment decides whether they are right. An onset of intrinsic coherence loss near 13 µg, the same for every material and every separation, with a second step at $\sqrt{3}$ times that mass, would support them; an onset elsewhere, or one that depends on density or separation, would refute them (Sections 5, 6, and 11).

The correction does not alter the motion. $\delta(m)$ is the lattice correction at $k_C = mc/\hbar$, a measure of how well the rest energy is represented. It is not a correction to the kinetic energy of the body's motion. At the wavenumber $k = mv/\hbar$ of a body moving at speed v, the same correction has relative size $\delta(m)(v/c)^2$, which is 3×10^{-18} for a 16.2 µg body at 1 m/s, and by Section 2.5, even this overstates the effect on a composite body. Mechanical frequencies, the dynamics of cantilevers and torsion balances, and the amplitude dependence searched for in tests of deformed commutators [25,26] are unchanged. In the parametrization of those tests, a correction of size $(pL/\hbar)^2/6$ has the form of a deformation with $\beta_0 = (L/\ell_P)^2/6 \approx 0.46$, while the oscillators of Ref. [26], of 20 µg and 77 µg, bound β_0, as they report it, only below 6×10^{12} and 5×10^{13} [*computed*].

What $\delta(m)$ does to an observable is not yet known. The model supplies no map from $\delta(m)$ to the energy shift of a specific mode (Section 9). Until that map is derived, the size of any reversible effect in the window is open, and the tests below rest on the thresholds themselves.

Any irreversible component was modeled in Ref. [16] by a phenomenological rate law,

$$\Gamma(m) = \begin{cases} 0, & m \le m_{\text{soft}}, \\ \Gamma_0\left[(m/m_{\text{soft}})^2 - 1\right]^2, & m_{\text{soft}} < m < m_{\text{hard}}, \end{cases} \qquad \Gamma_0 = \frac{\hbar}{mL^2}, \tag{2}$$

with coherence not sustained above m_{hard}. That paper treated the absolute scale Γ_0 as undetermined and called the vanishing below m_{soft} a modeling choice. Section 6 shows that the latter follows from P3, and Section 7 constrains the form of any irreversible component. Where a basis is needed, we read Γ as the decay rate of the coherence between neighboring energy levels of the collective excitation; for a channel linear in the Hamiltonian, this fixes the rate for every other pair of levels (Section 7). The irreversible part is treated as Markovian, as a phenomenological model; the Hermitian correction is static and produces no decoherence of its own. The lattice as a whole is a closed system with unitary dynamics. The center-of-mass excitation is a subsystem of it, so its reduced dynamics can be non-unitary; this is the sense in which the channel is open. The channel is trace-preserving and of Lindblad form, so the ordinary von Neumann and Rényi entropies apply to it. Generalized Rényi entropies have been developed for non-Hermitian evolution, in which the trace of the density matrix is not preserved [27,28]; they would be needed only if the lattice correction were non-Hermitian, which the model excludes. Throughout, we read the model as Ref. [16] constructs it, in which the lattice correction is Hermitian and loss of representability is the only intrinsic source of non-unitarity.

Rates, not oscillation frequencies. Two very large numbers appear in this paper. The Compton frequency $mc^2/\hbar = c/\ell_C$, about $10^{43}\,\text{s}^{-1}$ at m_{soft}, is the phase rate of the rest energy. It is not the frequency of any mechanical oscillation or electromagnetic wave, and it is relativistic by construction, since it comes from $E = mc^2$. The rate scale $\Gamma_0 = \hbar/(mL^2) = (\ell_C/L)\,c/L$ equals it at m_{soft}; it is a decay rate of coherence, not a frequency of motion. The mechanical frequencies relevant here, from the 1 Hz spring of Section 7 to

the gigahertz modes of acoustic resonators [29,30], are ordinary. The lattice correction to the motion is of order $\delta(m)(v/c)^2$, and the special-relativistic correction is of order $(v/c)^2$; both are negligible here. No new atomic, molecular, or optical physics enters: below m_{soft}, atoms, molecules, and light obey standard quantum mechanics. That the natural rate scale is so large is the point of Sections 7 and 8: experiments bound any intrinsic rate far below it.

4. The Collapse-Model Comparison

Collapse time. In standard quantum mechanics, a superposition does not collapse on its own; its coherence is lost only to the environment, by decoherence. Collapse models add an intrinsic, stochastic process that suppresses superpositions of different positions. The collapse time is the time on which this process removes the coherence between two branches: $\tau_{\text{DP}} = \hbar/E_G$ for DP and the inverse of the rate of Equation (4) for CSL. At the level of the density matrix, the effect is the same as decoherence, but its source is the dynamics itself, not an environment. The time is long for small masses and separations, which is why atoms and molecules behave quantum mechanically, and short for macroscopic bodies. The lattice model's counterpart is intrinsic decoherence, which vanishes below m_{soft}.

4.1. Diósi–Penrose

For a uniform sphere of mass m and radius R in a superposition of two positions a distance d apart, the DP energy is [31]

$$E_G = \frac{Gm^2}{R} \times \begin{cases} 2\eta^2 - \frac{3}{2}\eta^3 + \frac{1}{5}\eta^5, & \eta \le 1, \\ \frac{6}{5} - \dfrac{1}{2\eta}, & \eta \ge 1, \end{cases} \qquad \eta = \frac{d}{2R}, \tag{3}$$

with $\tau_{\text{DP}} = \hbar/E_G$. Equation (3) is Equation (23) of Ref. [31], written with the prefactor $6Gm^2/(5R)$ absorbed, and Appendix A derives it. We checked Equation (3) against a direct Fourier-space evaluation of the gravitational self-energy, which agrees to 0.01% for d/R from 10^{-3} to 8. For small separations, $E_G \to Gm^2d^2/(2R^3)$ [*computed*]. Throughout, R is the radius of the sphere itself, fixed by its mass and density, and the DP smearing length enters only through the bound quoted below.

Two limits matter below. For $d \ll R$, $E_G \approx \frac{2\pi}{3} G\, m\, \rho\, d^2$ with ρ the density. For $d \gg R$, $E_G \to \frac{6}{5}Gm^2/R$. For d below the atomic spacing, real matter concentrates its mass in nuclei, so the uniform sphere underestimates E_G unless the DP smearing length exceeds that spacing. The XENONnT search bounds the DP smearing length to $R_0 > 4.9 \times 10^{-10}$ m [6], larger than the atomic spacing, so the uniform sphere is close to the true value there as well. The DP times quoted below are upper bounds, or close to the true values, and the separations used for the material comparison of Section 5 lie above the atomic spacing.

4.2. Continuous Spontaneous Localization

In CSL, the decoherence rate between branches of a body separated by d is [4,5]

$$\Gamma_{\text{CSL}}(d) = \frac{\lambda}{m_0^2}\,(4\pi r_C^2)^{3/2} \int \frac{d^3k}{(2\pi)^3}\, e^{-k^2 r_C^2}\, |\tilde{\rho}(\mathbf{k})|^2 [1 - \cos(\mathbf{k}\cdot\mathbf{d})], \tag{4}$$

where m_0 is the nucleon mass and $\tilde{\rho}$ the Fourier transform of the mass density. For a single nucleon, it reduces to $\lambda[1 - e^{-d^2/(4r_C^2)}]$, which the script reproduces exactly [*computed*]. We take the standard $r_C = 10^{-7}$ m. Searches for spontaneous X-ray emission bound the rate from above [32], and the XENONnT detector has recently tightened the bound to $\lambda/r_C^2 < 3.0 \times 10^{-3}\,\text{s}^{-1}\text{m}^{-2}$ for white noise [6]. At $r_C = 10^{-7}$ m, this gives $\lambda < 3 \times 10^{-17}\,\text{s}^{-1}$, which excludes the originally proposed $\lambda = 10^{-16}\,\text{s}^{-1}$ [33]; free test masses give weaker bounds [34,35]. We quote CSL results at the largest allowed rate, $\lambda = 3 \times 10^{-17}\,\text{s}^{-1}$. Colored

or dissipative extensions of CSL, and larger r_C, remain less constrained [6]. CSL heats every body at [5]

$$\frac{dE}{dt} = \frac{3\lambda\hbar^2 m}{4m_0^2 r_C^2}, \tag{5}$$

which for 1 kg is about 9×10^{-18} W at that rate [*computed*].

5. First Discriminator: The Thresholds Depend on Mass Alone

Derivation. P3 makes representability a property of the center-of-mass excitation characterized by its total rest energy. The thresholds of Equation (1), the correction $\delta(m)$, and the rate law of Equation (2) are functions of m alone. Density, radius, shape, composition, and the separation Δx do not enter. The model assigns the same thresholds to every material (Section 2.5). [*derived*]

Contrast. Both collapse models depend on how the mass is distributed. At equal mass, the DP rate scales as the density for $d \ll R$ and as its cube root for $d \gg R$. The CSL rate scales as the density for $d \gg r_C$ and more steeply for $d \ll r_C$, where the surface of the body dominates. Table 1 gives the factor by which collapse is faster than for silica, for spheres of mass m_{soft}.

Table 1. Factor by which collapse is faster than for silica, for spheres of equal mass $m = m_{\text{soft}}$, in Diósi–Penrose (DP) and in CSL. The CSL factors do not depend on λ. The lattice model predicts identical thresholds and identical correction $\delta(m)$ for every row. For silica at $m = m_{\text{soft}}$, $R \approx 112\,\mu$m, so $d = 1$ mm is $d/R \approx 9$, not yet the limit $d \gg R$; this is why the DP factors at 1 mm still exceed the cube root of the density ratio.

Material	ρ (kg/m^3)	DP, 1 nm	DP, 1 mm	CSL, 1 nm	CSL, 1 mm
silica	2200	1.00	1.00	1.00	1.00
sapphire	3980	1.81	1.24	2.20	1.81
gold	19,300	8.77	2.17	18.1	8.76
osmium	22,590	10.27	2.29	22.3	10.25

The test is a ratio. Two bodies of equal mass and different density, in the same apparatus, either share their coherence limit or do not. It needs no absolute calibration, and it does not depend on the value of L. It is a test of what an observed coherence limit is. If a limit is found near the window, a mass-only onset supports the threshold reading and an onset that depends on density, or on Δx, at fixed mass refutes it. Ratios of CSL to DP rates that depend only on geometry have been studied for spheres with different radial mass profiles [36]; the comparison here adds a model whose thresholds have no material dependence at all.

6. Second Discriminator: No Intrinsic Decoherence Below m_{soft}

Derivation. The rate law of Equation (2) models the irreversible component of a failure of representability. Under P3, representability holds for every $m < m_{\text{soft}}$, so there is no failure. Since loss of representability is the model's only intrinsic source of non-unitarity (Section 3), there is nothing irreversible to model. The only lattice effect there is the Hermitian correction of Section 3, which generates unitary evolution and conserves purity. The lattice produces no intrinsic decoherence below m_{soft}, for any separation and at any time. The first line of Equation (2) states the same result. Within the representability-breakdown mechanism, it follows from P3 and needs no separate modeling choice [*derived*].

Contrast. Both collapse models predict a rate and no threshold, so every superposition eventually collapses. Figure 2 and Table 2 give the collapse times for silica spheres far below m_{soft}, each with the radius fixed by its mass and the density of silica.

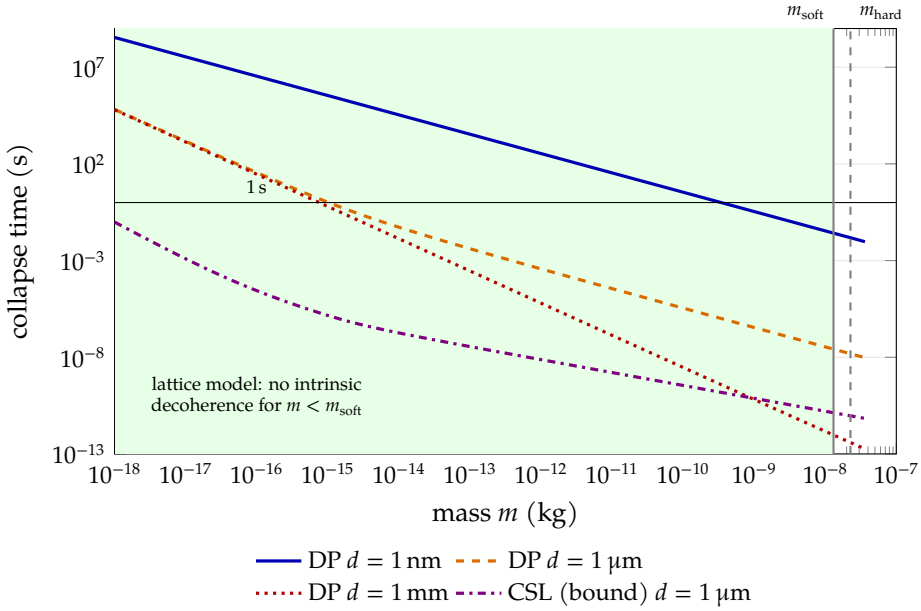


Figure 2. Collapse time for silica spheres: Diósi–Penrose, from Equation (3), at three separations, and CSL at the XENONnT bound, from Equation (4), at 1 µm. The shaded region, every mass below m_{soft}, is where the lattice model predicts no intrinsic decoherence at any time. The gray lines mark m_{soft} (solid) and m_{hard} (dashed). Each sphere's radius R in Equation (3) follows from its mass and the density of silica; it is not the DP smearing length bounded by XENONnT.

Table 2. Collapse times for silica spheres below m_{soft}, in Diósi–Penrose (DP) and in CSL at the XENONnT bound, $\lambda = 3 \times 10^{-17}\,\text{s}^{-1}$. Weaker CSL gives proportionally longer times. The lattice model predicts no intrinsic decoherence for every entry.

Mass	Model	$d = 1$ nm	$d = 1$ µm	$d = 1$ mm
10^{-15} kg	DP	3×10^{5} s	1.0 s	0.6 s
	CSL	0.3 s	1×10^{-6} s	1×10^{-6} s
1 ng	DP	3×10^{2} s	4×10^{-4} s	6×10^{-6} s
	CSL	3×10^{-3} s	8×10^{-9} s	1×10^{-9} s
1 µg	DP	0.3 s	3×10^{-7} s	7×10^{-11} s
	CSL	3×10^{-5} s	8×10^{-11} s	9×10^{-13} s

These masses lie between about 10 and 10^{7} times below m_{soft}, and Figure 2 extends the comparison to 10^{-18} kg. All of them lie above the present record for spatial superpositions, 2.9×10^{-22} kg (Section 10.1). The lightest are in the range targeted by space-based proposals [37], and all are far closer to present experiments than the threshold window. With environmental decoherence suppressed, coherence maintained beyond a collapse model's predicted time would falsify that model, and intrinsic decoherence observed there would falsify the lattice model. This is a test of the model that does not require reaching the threshold window.

Below m_{soft}, the lattice model agrees with standard quantum mechanics, which also predicts no intrinsic decoherence. The test can falsify the lattice model and can exclude collapse models, but a null result does not confirm the lattice model over standard quantum mechanics. The model's distinctive positive content remains the thresholds.

Energy-driven reduction. Models of energy-driven stochastic reduction [12–14] and intrinsic decoherence [15] dephase superpositions of different energies at a rate that grows with the energy spread, at every mass. They predict finite dephasing of energy superpositions below m_{soft}, for example, of a cat state of a light mechanical mode, where the lattice

model predicts none. The second discriminator also separates the lattice model from this class, which the heating and reversibility tests below do not.

Resolving an intrinsic rate. A collapse time alone does not show that an effect can be resolved against environmental decoherence, from gas collisions, blackbody radiation, and technical noise. What matters is how precisely an experiment can estimate an intrinsic rate in the presence of these. Quantum estimation theory gives the attainable precision for DP-type decoherence in mechanical systems and the probe states that reach it [38]. For the null test, the requirement is that the environmental rate be known well enough that the collapse-model rate would stand out. For the 10^{-15} kg example over 1 µm, CSL at its bound must be resolved at about $10^{6}\,\mathrm{s}^{-1}$ and DP at about $1\,\mathrm{s}^{-1}$; the lattice model predicts no excess at either level.

7. Third Discriminator: No Anomalous Heating or Radiation

7.1. Microscopic Matter

Every atom, nucleon, and electron lies far below m_{soft}. By Section 6, no irreversible channel acts on them, so the lattice model predicts no spontaneous radiation from ordinary matter. This is consistent with the underground X-ray searches that excluded the parameter-free version of DP [39] and bound CSL from above [6,32], since both models produce such radiation. CSL also heats bulk matter, by Equation (5), at up to about 9×10^{-18} W per kilogram at its present bound. Non-interferometric tests bound exactly this heating, with ultracold cantilevers [8,9], layered force sensors [10], levitated systems [7], and free test masses in space [11,35]; the lattice model predicts no excess in any of them [*derived*].

7.2. A General Condition for Heating

Consider a Markovian irreversible channel in Lindblad form [40], with operator $\hat{L}$ and rate γ. An observable $\hat{A}$ evolves as

$$\frac{d\langle \hat{A} \rangle}{dt} \supset \gamma \left\langle \hat{L}^{\dagger} \hat{A} \hat{L} - \tfrac{1}{2}\{\hat{L}^{\dagger}\hat{L}, \hat{A}\} \right\rangle, \tag{6}$$

which vanishes when $\hat{L}$ commutes with $\hat{A}$. Three cases fix what the model can be. A channel diagonal in the Hamiltonian of the collective excitation, $\hat{L} = f(\hat{H})$, commutes with it, free or in a trap, and produces no heating at all. A function of momentum alone does the same for a free body, but in a trap, the potential breaks the commutation: for $\hat{L} = (L\hat{p}/\hbar)^2$ at rate Γ_0, the heating is $2\omega^2 L^2 \langle p^2 \rangle / \hbar$, suppressed by L^2 to about 2×10^{-54} W for a 1 kg body on a 1 Hz spring at room temperature. A position-localizing channel, such as those of collapse models [5], does not commute with the kinetic energy; for $\hat{L} = \hat{x}$, it heats at $\gamma\hbar^2/(2m)$. We confirmed these statements numerically, on a discretized free particle and on a truncated oscillator [*derived*].

The model's channel is the first. P3 concerns the energy of the collective excitation, its rest energy together with the energy of its motion, so the basis in which representability can fail is the excitation's own energy basis. For a trapped body or an acoustic mode, that Hamiltonian includes the confining potential, because the potential fixes the excitation's energy levels. For a free body, it reduces to a function of $p^2/2m$. The momentum channel above serves only as a contrast.

7.3. A Consistency Requirement on the Model

Above m_{hard}, the model states that coherence is not sustained, with rate scale $\Gamma_0 = \hbar/(mL^2)$. Every macroscopic body lies above m_{hard}, so the form of this channel is constrained by the absence of anomalous heating in ordinary matter. Suppose the channel localized position on the lattice scale L. It would then drive momentum diffusion at

$\Gamma_0 h^2/L^2$, and a 1.93 kg free test mass would heat at about 3×10^{35} W. The LISA Pathfinder force-noise level, of order 10^{-15} N Hz$^{-1/2}$ [41], limits the rate of any such channel to below about 3×10^{-32} s^{-1}. That is 66 orders of magnitude below Γ_0 [*computed*]. Rotational noise of the same mission tightens collapse-model bounds further [42], which only strengthens this conclusion.

7.4. A Second Consistency Requirement: Classical Phase Stability

An energy-dephasing channel does not heat, but it is not free of consequences. Coherence between neighboring energy levels of an oscillator is what gives its motion a definite phase. For $\hat{L} \propto \hat{H}$, a coherent state's amplitude $\langle \hat{a} \rangle$ decays at the rate at which neighboring-level coherence decays, while its energy is unchanged; in a single run, the oscillator is driven toward an energy eigenstate, which does not oscillate. A pendulum with a bob above m_{hard} is a center-of-mass excitation to which P3 applies. At the terminal rate of Ref. [16], $4\Gamma_0 \approx 6 \times 10^{35}$ s^{-1} for 1 kg, its phase would be lost at once. A pendulum clock with a seconds pendulum, of period 2 s, that keeps time to about a second a day limits the phase-diffusion rate to about 10^{-4} s^{-1}, nearly 40 orders of magnitude below that rate [*computed*].

Together with the first requirement, this restricts what the hard threshold can be. The loss of representability above m_{hard} can be neither position localization at the lattice scale nor strong dephasing between neighboring energy levels. The thresholds and the $\sqrt{3}$ ratio are unaffected, but the published rate scale cannot apply to either form. A microscopic derivation of the breakdown must satisfy both requirements [*derived consistency requirement*].

7.5. What Then Loses Coherence?

A channel diagonal in the Hamiltonian leaves the energy distribution unchanged. For a free particle, it also leaves the momentum distribution unchanged, including the far-field interference fringes of a spatial superposition; this too was confirmed numerically. In the window, the lattice model allows only dephasing between different energy components of the collective excitation, in the spirit of energy-basis intrinsic decoherence [15], not loss of spatial fringes. The appropriate test is a state with coherence between distinct energy components, such as the mechanical cat states of a resonator [29], not matter-wave interferometry. This leaves the thresholds and the $\sqrt{3}$ ratio unchanged and changes only the observable that would reveal them.

Scope. The heating test and the reversibility test of Section 9 separate the lattice model from position-localizing collapse models such as DP and CSL. They do not separate it from energy-driven reduction, which also dephases in the energy basis, conserves energy, and does not heat. Against that class, the distinguishing tests are the null below m_{soft} (Section 6) and the mass-only onset (Section 5).

A fifth discriminator: phonon-number statistics. The two channel types act differently on the distribution of phonon numbers of a mechanical mode. A position-localizing channel heats the mode and reshapes the distribution. An energy-dephasing channel leaves every phonon-number probability exactly unchanged because it is diagonal in that basis. Phonon counting, already available in resonators coupled to superconducting qubits [29,43], tells the two apart at any mass, far below the window as well as in it [*derived*].

8. A Conditional Constraint from an Existing Experiment

Section 7 implies that any irreversible lattice effect in the window acts as dephasing between energy components of the excitation. Mechanical cat states containing coherence between distinct oscillator-energy components have been made. Bild et al. [29] prepared cat states of a bulk acoustic mode of a sapphire resonator, superpositions of two opposite-phase coherent states. The two components have the same mean energy, but the superposition

carries coherence among the oscillator's energy eigenstates, which an energy-dephasing channel would destroy.

What was observed? The cats had mean phonon numbers up to about 2.6. Their interference features decayed on a timescale of about 10 µs, measured over waiting times up to 40 µs, against a phonon energy-relaxation time of 84 µs [29]. A companion analysis of the same resonator followed the Wigner negativity of Fock states for up to 40 µs and quoted a macroscopicity of $\mu = 11.3$ [43], in the measure of Nimmrichter and Hornberger [44]. The same cat data give a bound on the DP smearing length [45]. Fock states with up to six phonons and genuine quantum non-Gaussianity have since been prepared in a resonator of the same type, with the same quoted effective mass [46].

Which mass? The effective mass of an acoustic mode depends on the displacement used to define it. Bild et al. quote 16.2 µg, from the root-mean-square atomic displacement, and 1.0 µg from the maximum displacement [29]; the companion analysis uses 1.0 µg [43]. The crystal's center of mass does not move, so the mode is not a center-of-mass excitation in the strict sense of P3. Whether internal vibrations can stay quantum while the center of mass is classical has been examined in a related model [18]. Whether P3 applies to it, and with which mass, is an assumption. With 16.2 µg, the mode lies inside the window; with 1.0 µg, it lies in the null regime of Section 6. In the measure of Nimmrichter and Hornberger, which rates a state by the mass and time over which it tests quantum mechanics, the companion analysis takes 1.0 µg as the operative mass [43]. On that operational reading, the mode lies below the threshold.

The bound. At $m = 16.2$ µg, $m/m_{\text{soft}} = 1.239$, and the rate law of Equation (2) at its full scale gives $\Gamma_0[(m/m_{\text{soft}})^2 - 1]^2 \approx 2.6 \times 10^{42}\,\text{s}^{-1}$. The observed coherence requires an intrinsic rate below about $1/(10\,\mu\text{s}) = 10^5\,\text{s}^{-1}$. With Γ read as the neighboring-level rate of Section 3, the cat's coherence decays faster by a factor of order its phonon number, which changes this figure by less than one order. If P3 applies to this mode with the root-mean-square mass, the irreversible coupling in the window must lie at least 37 orders of magnitude below its natural scale. The intermediate regime then cannot be governed by the original full-strength irreversible rate, and the window is in practice reversible [*computed*].

The caveat. The bound holds only if P3 applies to this mode with the root-mean-square mass. With the other convention, the experiment lies in the null regime, where the model predicts no intrinsic decoherence, and it is again consistent with the model. In both cases, the experiment is compatible with the threshold framework; the constraint is conditional, and a test of whole-body motion in the window would remove the ambiguity [*open*].

9. A Fourth Signature: Reversibility

The Hermitian lattice correction is time independent. If it shifts the energy of a mode, on a superposition of two energy levels, it produces a static, deterministic relative phase. For a two-level encoding in which a π pulse reverses that relative phase, a Hahn-echo sequence cancels it, whereas irreversible dephasing is not restored. A static correction is the opposite of a Markovian channel: it is perfectly correlated in time, which is why an echo removes it. The window effect would be a pure phase that preserves contrast and vanishes under an echo; collapse models produce a loss of contrast that no echo restores, accompanied by heating [*derived*]. The size of this phase for a given experiment is not yet predicted because the model supplies no map from $\delta(m)$ to the energy shift of a specific mode [*open*]. Deriving that map, an energy shift $\Delta E(m, \omega, \ldots)$ for a given mode, is the next calculation the model needs; until then, the reversibility test is a signature to look for, not a prediction of a definite size.

https://doi.org/10.3390/quantum8040117

10. Experimental Outlook

10.1. Where Experiments Stand

Table 3 places the predictions against present experiments. The largest masses brought into spatial superposition are sodium nanoclusters of about 172 kDa, or 2.9×10^{-22} kg, in matter-wave interferometry [47], after molecules beyond 25 kDa in 2019 [24]. Levitated silica nanoparticles of about 10^{-18} kg have been cooled to their motional ground state, from room temperature [48] and in cryogenic free space [49], but have not yet been delocalized over distances comparable to their size. The largest coherence length reached so far, about 73 pm for a sphere of 100 nm diameter cooled to its ground state, is far below that size [50]. The two spheres of the worked example below are $10^{4.5}$ and $10^{6.5}$ times heavier than the record superposition. The acoustic-mode cat states of Section 8 lie inside the threshold window, or below it, depending on the mass convention. At the other extreme, the center-of-mass motion of a 10 kg mirror has been cooled to an average occupation of 10.8 [51], at a mass far above m_{hard}. That state is thermal, with no coherence between energy components, so it does not test the window; it shows that such masses can be brought close to the quantum regime. [*computed*]

Table 3. Present experiments, by mass, and the parts of this paper they bear on.

Platform	Mass	Achieved	Bears on
sodium nanoclusters [47]	2.9×10^{-22} kg	spatial superposition; mass record	collapse-model bounds
levitated silica sphere [48,49]	$\sim 10^{-18}$ kg	motional ground state; no spatial superposition yet	second discriminator; worked example
acoustic-mode cat [29,43]	16.2 µg (rms) or 1.0 µg (max), effective	cat states, coherence about 10 µs	the window or the null regime (Section 8)
bulk acoustic resonator [30]	microgram-scale modes	classical phonon coherence 6.2 ms	platform for the window tests
gravitational-wave mirror [51]	10 kg	thermal occupation 10.8	above m_{hard}; no coherence test

10.2. The Discriminators at a Glance

Table 4 summarizes the discriminators and the experiments that address them.

The second discriminator is the most practical because its prediction applies at masses far closer to present experiments than the threshold window. The first needs no absolute calibration because it is a ratio. The third is already consistent with existing null results; it and the fourth separate the model from DP and CSL but not from energy-driven reduction (Section 7).

Table 4. The discriminators, with the predictions of each model and the experiments that address them.

Discriminator	Lattice Model	Diósi–Penrose	CSL	Test
equal mass, different density	identical thresholds	rate $\propto \rho$ $(d \ll R)$, $\rho^{1/3}$ $(d \gg R)$	rate $\propto \rho$ $(d \gg r_C)$, steeper below	same apparatus, two materials
below m_{soft}	no intrinsic decoherence	1 s at 10^{-15} kg, 1 µm	$\approx$1 µs at 10^{-15} kg, 1 µm	levitated particles [37,48,49]

Table 4. *Cont*.

Discriminator	Lattice Model	Diósi–Penrose	CSL	Test
heating and radiation	none measurable	radiation; parameter-free form excluded [39]	heating and radiation; original strength excluded [6]	radiation searches; free test masses [41]; cantilevers [9,10]
reversibility	pure phase, removed by echo (size open)	contrast loss	contrast loss	echo on states with energy coherence [29]
phonon statistics	distribution unchanged	heating reshapes it	heating reshapes it	phonon counting [29,43]

10.3. Prospects with Near-Future Data

Near-future data bear on the lattice model and on collapse models in different ways, and Table 5 sets out the margins.

Radiation searches. XENONnT improved the previous bounds on CSL by two orders of magnitude and on DP by a factor of five [6]. Next-generation xenon observatories plan about ten times its target mass [52]. For a background-limited search the sensitivity grows roughly as the square root of the exposure, so a further factor of a few is a reasonable expectation; this is our estimate, not a published projection. Germanium searches at Gran Sasso and in the Majorana Demonstrator test the same radiation [32,39,53]. Each improvement tightens CSL and DP. The lattice model predicts no signal at any sensitivity, so these searches can refute it only by finding a signal that a collapse model must then explain.

Heating. Non-interferometric tests already bound CSL heating with cantilevers, at $\lambda < 2 \times 10^{-10}\,\mathrm{s}^{-1}$ for $r_C = 10^{-7}\,\mathrm{m}$, and a proposed parametric-heating test of a levitated nanosphere could reach $\lambda \sim 10^{-12}\,\mathrm{s}^{-1}$ [7]. These are weaker than the X-ray bound at the standard r_C but stronger at larger r_C and for colored noise. The lattice model predicts no heating, so a heating signal would favor a position-localizing model, and phonon-number statistics (Section 7) would identify the channel.

Interferometry. The record spatial superposition is $2.9{\times}10^{-22}$ kg [47], about 13.7 orders of magnitude below m_{soft}. Testing white-noise CSL at its bound needs the first sphere of the worked example (Section 10.4), 9×10^{-18} kg, held for about 10 ms; reaching GRW strength interferometrically needs about 10^7 u over 180 nm for about 20 s [7]. The null test of Section 6 applies already to that first sphere, far below the window.

Mechanical quantum states. Bulk acoustic resonators of the same family as that of Section 8 now reach classical phonon coherence times of 6.2 ms with negligible pure dephasing [30], about 600 times the cat coherence time used in Section 8. If quantum states of comparable lifetime are prepared, the conditional bound tightens by almost three orders of magnitude, and the echo and phonon-counting tests become practical on the same platform.

Table 5. Near-future data and what they test. The lattice model predicts no signal in the first three rows; its distinctive tests are the null below m_{soft} and the behavior near the window.

Platform	Present Reach	Near-Future Margin and What It Tests
xenon and germanium radiation searches	CSL $\lambda < 3 \times 10^{-17}\,\mathrm{s}^{-1}$; DP $R_0 > 4.9 \times 10^{-10}\,\mathrm{m}$ [6]	a factor of a few (our estimate); tightens CSL and DP, no lattice signal
cantilevers, levitated heating	$\lambda < 2 \times 10^{-10}\,\mathrm{s}^{-1}$ [7]	to $\sim 10^{-12}\,\mathrm{s}^{-1}$ proposed [7]; heating channels

Table 5. *Cont*.

Platform	Present Reach	Near-Future Margin and What It Tests
free test masses	LISA Pathfinder [41,42]	LISA; consistency requirement of Section 7
matter-wave and levitated superpositions	2.9×10^{-22} kg [47]	10^{-17}–10^{-15} kg; the null test, CSL, and DP
mechanical cats and Fock states	coherence ∼10 µs [29]	ms lifetimes [30]; window bound, echo, phonon counting

10.4. A Worked Example

Table 6 gives the predictions for two levitated silica spheres. The first, of radius 100 nm, is within an order of magnitude of the mass of the ground-state-cooled particles of Refs. [48,49]; holding its superposition for 10 ms would test white-noise CSL at its largest allowed rate, while DP would need hours. The second, of 10^{-15} kg, is a goal of space-based proposals [37]; holding it for several seconds would exclude both collapse models. For both spheres, the three models give distinct outcomes: decoherence at the CSL time, decoherence at the DP time, or none [*computed*]. Whether such a rate can be resolved against environmental decoherence is discussed in Section 6.

Table 6. Predicted intrinsic collapse times for two levitated silica spheres. The lattice model predicts no intrinsic decoherence in either case.

Sphere	Separation	DP	CSL, XENONnT Bound
$R = 100$ nm, 9.2×10^{-18} kg	100 nm	6×10^{3} s	8×10^{-3} s
$R = 480$ nm, 10^{-15} kg	1 µm	1.0 s	1×10^{-6} s

11. Discussion

Consequences for the threshold model. Four points refine Ref. [16] without changing its thresholds or its $\sqrt{3}$ ratio. The vanishing of the irreversible rate below m_{soft} follows from P3, given the model's reading in Section 3; it is not a separate modeling choice. The irreversible component cannot be position localization at the stated rate scale, and on the natural reading, it is dephasing in the energy basis; even that cannot be strong above m_{hard} because classical oscillations keep their phase. On that reading, and if P3 applies to the mode of Ref. [29] with its root-mean-square mass, the window is effectively reversible. The Compton-scale correction $\delta(m)$ does not alter the motion of microgram bodies, and its observable consequence is open. The first three follow from P3 and that reading; the second also uses the Markovian treatment of the channel, and the third the effective-mass assumption of Section 8.

What would falsify the model? Below m_{soft}: Intrinsic decoherence of a center-of-mass superposition, once environmental sources are accounted for, refutes the model; its absence cannot confirm it over standard quantum mechanics. In the window: An onset of coherence loss whose mass scale depends on density, or on Δx, at fixed mass refutes the threshold reading, and a mass-only onset at the predicted masses, in the ratio $\sqrt{3}$, would support it. The irreversible part is already bounded, conditionally, at 37 orders below its natural scale. Above m_{hard}: The published statement that coherence is not sustained has no fixed observable until the breakdown is derived. Its form is restricted by the two consistency requirements of Section 7, and a derived channel that violates either is ruled out. If the hard threshold is read as the loss of superpositions of macroscopically distinct center-of-mass states, a sustained superposition of that kind above m_{hard} refutes it.

Dependence on the bond length. The absolute window depends on L, which is tied to one calibration. The first and third discriminators and the fourth signature do not depend on L in form; the 66-order margin of Section 7 scales as L^{-4} and moves by less than one order for any L up to $2.8\,\ell_P$, a check printed by the script. The second depends on L through the location of m_{soft}, which stays above every mass in Table 2 for any L up to $2.8\,\ell_P$, where $m_{\text{soft}} = 7.8\,\mu\text{g}$.

Limitations. P3 is a hypothesis, not a theorem, and every discriminator here inherits that status; Section 2.5 states what it assumes. The DP estimates use uniform spheres; below the atomic scale, they are upper bounds on the collapse time, or close to it. The CSL figures assume white noise and $r_C = 10^{-7}$ m, at the present XENONnT bound; colored or dissipative extensions weaken the X-ray bounds [5,6]. The analysis of heating assumes a Markovian channel. A microscopic, operator-level derivation of the representability breakdown would fix the size of the reversible phase and the absolute rate, and remains open.

12. Conclusions

The lattice model and collapse models predict limits on macroscopic coherence, but they differ in kind. The lattice threshold depends on mass alone, the same for every material; it permits no intrinsic decoherence below 13.1 µg at any time, which also separates it from energy-driven reduction; and it produces no measurable heating or radiation. The last is also a consistency requirement, which shows that P3 cannot mean position localization at the lattice scale; the model's loss of coherence above its threshold must be, to any measurable extent, dephasing between energy components, not loss of spatial fringes, and the phase stability of classical oscillators limits even that. The Compton-scale correction leaves the motion of microgram bodies unchanged. An existing mechanical cat state does not conflict with the threshold framework and, if P3 applies to its root-mean-square effective mass of 16.2 µg, constrains the irreversible coupling in the intermediate window to at least 37 orders of magnitude below the nominal rate scale. In the other common convention, the mode lies below the threshold. The most accessible test lies far below the threshold window, where collapse models predict decoherence within a second or much less, and the lattice model, like standard quantum mechanics, predicts none.

Funding: This research received no external funding.

Data Availability Statement: No new datasets were generated. A Python 3 script that reproduces every number in this paper (46 labeled checks, NumPy only; tested with Python 3.13 and NumPy 2.5) is available at https://github.com/raghu91302/ssmtheory/raw/main/discriminator_scripts.zip (accessed on 1 November 2026).

Conflicts of Interest: Author Raghu Kulkarni was employed by the company IDrive Inc. The author declares that the research was conducted in the absence of any commercial or financial relationships that could be construed as a potential conflict of interest.

Appendix A. The Diósi–Penrose Energy of a Uniform Sphere

Penrose's energy for a superposition of two mass distributions ρ_1 and ρ_2 is

$$E_G = \frac{G}{2}\iint \frac{[\rho_1(\mathbf{x}) - \rho_2(\mathbf{x})][\rho_1(\mathbf{y}) - \rho_2(\mathbf{y})]}{|\mathbf{x} - \mathbf{y}|}\, d^3x\, d^3y.$$

For two copies of one uniform sphere displaced by d, write $I(d) = G\iint \rho(\mathbf{x})\rho(\mathbf{y} + \mathbf{d})/|\mathbf{x} - \mathbf{y}|\, d^3x\, d^3y$ for the magnitude of their mutual gravitational energy. Expanding the product gives $E_G = I(0) - I(d)$. The self-term is $I(0) = 6Gm^2/(5R)$, twice the gravitational self-energy of the sphere. For separated spheres, $d \geq 2R$, the mutual energy is that of two point masses,

$I(d) = Gm^2/d$, which gives the second line of Equation (3) with $\eta = d/(2R)$. For overlapping spheres, integrating the potential of one sphere over the volume of the other gives

$$I(d) = \frac{Gm^2}{R}\left(\frac{6}{5} - 2\eta^2 + \frac{3}{2}\eta^3 - \frac{1}{5}\eta^5\right), \qquad \eta \le 1,$$

which gives the first line. The two lines agree at $\eta = 1$, where both equal $0.7\,Gm^2/R$, and the first reduces to $Gm^2d^2/(2R^3)$ for small d. The same result is Equation (23) of Ref. [31]. The script checks it against a direct Fourier-space evaluation.

References

1. Diósi, L. A universal master equation for the gravitational violation of quantum mechanics. *Phys. Lett. A* **1987**, *120*, 377–381. [CrossRef]
2. Diósi, L. Models for universal reduction of macroscopic quantum fluctuations. *Phys. Rev. A* **1989**, *40*, 1165. [CrossRef] [PubMed]
3. Penrose, R. On gravity's role in quantum state reduction. *Gen. Relativ. Gravit.* **1996**, *28*, 581–600. [CrossRef]
4. Ghirardi, G.C.; Pearle, P.; Rimini, A. Markov processes in Hilbert space and continuous spontaneous localization of systems of identical particles. *Phys. Rev. A* **1990**, *42*, 78. [CrossRef] [PubMed]
5. Bassi, A.; Lochan, K.; Satin, S.; Singh, T.P.; Ulbricht, H. Models of wave-function collapse, underlying theories, and experimental tests. *Rev. Mod. Phys.* **2013**, *85*, 471. [CrossRef]
6. Aprile, E.; Aalbers, J.; Abe, K.; Ahmed Maouloud, S.; Althueser, L.; Andrieu, B.; Angelino, E.; Antón Martin, D.; Armbruster, S.R.; Arneodo, F.; et al. Challenging spontaneous quantum collapse with the XENONnT dark matter detector. *Phys. Rev. Lett.* **2026**, *136*, 120201. [CrossRef] [PubMed]
7. Carlesso, M.; Donadi, S.; Ferialdi, L.; Paternostro, M.; Ulbricht, H.; Bassi, A. Present status and future challenges of non-interferometric tests of collapse models. *Nat. Phys.* **2022**, *18*, 243–250. [CrossRef]
8. Vinante, A.; Bahrami, M.; Bassi, A.; Usenko, O.; Wijts, G.H.; Oosterkamp, T.H. Upper bounds on spontaneous wave-function collapse models using millikelvin-cooled nanocantilevers. *Phys. Rev. Lett.* **2016**, *116*, 090402. [CrossRef] [PubMed]
9. Vinante, A.; Mezzena, R.; Falferi, P.; Carlesso, M.; Bassi, A. Improved noninterferometric test of collapse models using ultracold cantilevers. *Phys. Rev. Lett.* **2017**, *119*, 110401. [CrossRef] [PubMed]
10. Vinante, A.; Carlesso, M.; Bassi, A.; Chiasera, A.; Varas, S.; Falferi, P.; Margesin, B.; Mezzena, R.; Ulbricht, H. Narrowing the parameter space of collapse models with ultracold layered force sensors. *Phys. Rev. Lett.* **2020**, *125*, 100404. [CrossRef] [PubMed]
11. Gasbarri, G.; Belenchia, A.; Carlesso, M.; Donadi, S.; Bassi, A.; Kaltenbaek, R.; Paternostro, M.; Ulbricht, H. Testing the foundation of quantum physics in space via interferometric and non-interferometric experiments with mesoscopic nanoparticles. *Commun. Phys.* **2021**, *4*, 155. [CrossRef]
12. Percival, I.C. Primary state diffusion. *Proc. R. Soc. Lond. A* **1994**, *447*, 189–209. [CrossRef]
13. Hughston, L.P. Geometry of stochastic state vector reduction. *Proc. R. Soc. Lond. A* **1996**, *452*, 953–979. [CrossRef]
14. Adler, S.L.; Brody, D.C.; Brun, T.A.; Hughston, L.P. Martingale models for quantum state reduction. *J. Phys. A* **2001**, *34*, 8795. [CrossRef]
15. Milburn, G.J. Intrinsic decoherence in quantum mechanics. *Phys. Rev. A* **1991**, *44*, 5401. [CrossRef] [PubMed]
16. Kulkarni, R. A two-step quantum–classical threshold at 13.1–22.6 µg with exact ratio $\sqrt{3}$ from a close-packed vacuum lattice. *Quantum Rep.* **2026**, *8*, 78. [CrossRef]
17. Aguiar, G.H.S.; Matsas, G.E.A. Will we ever quantize the center of mass of macroscopic systems? A case for a Heisenberg cut in quantum mechanics. *arXiv* **2026**, arXiv:2601.20525. [CrossRef]
18. Aguiar, G.H.S.; Matsas, G.E.A. Quantum internal vibrations in macroscopic systems with classical centers of mass. *arXiv* **2025**, arXiv:2509.22429. [CrossRef]
19. Kulkarni, R. Matter as incomplete crystallization: Quark charges, color confinement, and the proton mass from a single extra node in the vacuum lattice. *Phys. Open* **2026**, *27*, 100423. [CrossRef]
20. Kulkarni, R. Defect migration in the D_4 vacuum lattice: Hop parity, site symmetry, and soliton kinematics. *Symmetry* **2026**, *18*, 1571. [CrossRef]
21. Kulkarni, R. A 67%-rate CSS code on the FCC lattice: $[[192, 130, 3]]$ from weight-12 stabilizers. *arXiv* **2026**, arXiv:2603.20294. [CrossRef]
22. Hossenfelder, S. Minimal length scale scenarios for quantum gravity. *Living Rev. Relativ.* **2013**, *16*, 2. [CrossRef] [PubMed]
23. Hossenfelder, S. The soccer-ball problem. *SIGMA* **2014**, *10*, 074. [CrossRef]
24. Fein, Y.Y.; Geyer, P.; Zwick, P.; Kiałka, F.; Pedalino, S.; Mayor, M.; Gerlich, S.; Arndt, M. Quantum superposition of molecules beyond 25 kDa. *Nat. Phys.* **2019**, *15*, 1242–1245. [CrossRef]

25. Pikovski, I.; Vanner, M.R.; Aspelmeyer, M.; Kim, M.S.; Brukner, Č. Probing Planck-scale physics with quantum optics. *Nat. Phys.* **2012**, *8*, 393–397. [CrossRef]
26. Bawaj, M.; Biancofiore, C.; Bonaldi, M.; Bonfigli, F.; Borrielli, A.; Di Giuseppe, G.; Marconi, L.; Marino, F.; Natali, R.; Pontin, A.; et al. Probing deformed commutators with macroscopic harmonic oscillators. *Nat. Commun.* **2015**, *6*, 7503. [CrossRef] [PubMed]
27. Li, D.; Zheng, C. Non-Hermitian generalization of Rényi entropy. *Entropy* **2022**, *24*, 1563. [CrossRef] [PubMed]
28. Liu, Z.; Zheng, C. Non-Hermitian quantum Rényi entropy dynamics in anyonic-PT symmetric systems. *Symmetry* **2024**, *16*, 584. [CrossRef]
29. Bild, M.; Fadel, M.; Yang, Y.; von Lüpke, U.; Martin, P.; Bruno, A.; Chu, Y. Schrödinger cat states of a 16-microgram mechanical oscillator. *Science* **2023**, *380*, 274–278. [CrossRef] [PubMed]
30. Luo, Y.; Diamandi, H.H.; Li, H.; Bi, R.; Mason, D.; Yoon, T.; Guo, X.; Tang, H.; Behunin, R.O.; Walker, F.J.; et al. Millisecond coherence times in gigahertz-frequency mechanical oscillators. *Nat. Phys.* **2026**, *22*, 1486–1492. [CrossRef]
31. Howl, R.; Penrose, R.; Fuentes, I. Exploring the unification of quantum theory and general relativity with a Bose–Einstein condensate. *New J. Phys.* **2019**, *21*, 043047. [CrossRef]
32. Piscicchia, K.; Bassi, A.; Curceanu, C.; Del Grande, R.; Donadi, S.; Hiesmayr, B.C.; Pichler, A. CSL collapse model mapped with the spontaneous radiation. *Entropy* **2017**, *19*, 319. [CrossRef]
33. Ghirardi, G.C.; Rimini, A.; Weber, T. Unified dynamics for microscopic and macroscopic systems. *Phys. Rev. D* **1986**, *34*, 470. [CrossRef] [PubMed]
34. Carlesso, M.; Bassi, A.; Falferi, P.; Vinante, A. Experimental bounds on collapse models from gravitational wave detectors. *Phys. Rev. D* **2016**, *94*, 124036. [CrossRef]
35. Helou, B.; Slagmolen, B.J.J.; McClelland, D.E.; Chen, Y. LISA Pathfinder appreciably constrains collapse models. *Phys. Rev. D* **2017**, *95*, 084054. [CrossRef]
36. Davila, R.; Milburn, G.J. Geometry-only CSL/DP ratios and the nonuniqueness of decoherence kernels. *arXiv* **2026**, arXiv:2608.05972. [CrossRef]
37. Kaltenbaek, R.; Hechenblaikner, G.; Kiesel, N.; Romero-Isart, O.; Schwab, K.C.; Johann, U.; Aspelmeyer, M. Macroscopic quantum resonators (MAQRO): Testing quantum and gravitational physics with massive mechanical resonators. *Exp. Astron.* **2012**, *34*, 123–164. [CrossRef]
38. Souza, L.A.M.; Neto, O.P.d.; Russo, E.; Franco, R.L.; Adesso, G. Gravitational decoherence estimation in optomechanical systems. *Phys. Rev. A* **2026**, *114*, 022442. [CrossRef]
39. Donadi, S.; Piscicchia, K.; Curceanu, C.; Diósi, L.; Laubenstein, M.; Bassi, A. Underground test of gravity-related wave function collapse. *Nat. Phys.* **2021**, *17*, 74. [CrossRef]
40. Lindblad, G. On the generators of quantum dynamical semigroups. *Commun. Math. Phys.* **1976**, *48*, 119–130. [CrossRef]
41. Armano, M.; Audley, H.; Baird, J.; Binetruy, P.; Born, M.; Bortoluzzi, D.; Castelli, E.; Cavalleri, A.; Cesarini, A.; Cruise, A.M.; et al. Beyond the required LISA free-fall performance: New LISA Pathfinder results down to 20 μHz. *Phys. Rev. Lett.* **2018**, *120*, 061101. [CrossRef] [PubMed]
42. Altamura, D.G.A.; Vinante, A.; Carlesso, M. Improved bounds on collapse models from rotational noise of the Laser Interferometer Space Antenna Pathfinder mission. *Phys. Rev. A* **2025**, *111*, L020203. [CrossRef]
43. Schrinski, B.; Yang, Y.; von Lüpke, U.; Bild, M.; Chu, Y.; Hornberger, K.; Nimmrichter, S.; Fadel, M. Macroscopic quantum test with bulk acoustic wave resonators. *Phys. Rev. Lett.* **2023**, *130*, 133604. [CrossRef] [PubMed]
44. Nimmrichter, S.; Hornberger, K. Macroscopicity of mechanical quantum superposition states. *Phys. Rev. Lett.* **2013**, *110*, 160403. [CrossRef] [PubMed]
45. Fadel, M. Probing gravity-related decoherence with a 16 μg Schrödinger cat state. *arXiv* **2023**, arXiv:2305.04780. [CrossRef]
46. Rahman, Q.R.; Kladarić, I.; Kern, M.-E.; Lachman, L.; Chu, Y.; Filip, R.; Fadel, M. Genuine quantum non-Gaussianity and metrological sensitivity of Fock states prepared in a mechanical resonator. *arXiv* **2024**, arXiv:2412.20971. [CrossRef]
47. Pedalino, S.; Ramírez-Galindo, B.E.; Ferstl, R.; Hornberger, K.; Arndt, M.; Gerlich, S. Probing quantum mechanics with nanoparticle matter-wave interferometry. *Nature* **2026**, *649*, 866–870. [CrossRef] [PubMed]
48. Delić, U.; Reisenbauer, M.; Dare, K.; Grass, D.; Vuletić, V.; Kiesel, N.; Aspelmeyer, M. Cooling of a levitated nanoparticle to the motional quantum ground state. *Science* **2020**, *367*, 892–895. [CrossRef] [PubMed]
49. Tebbenjohanns, F.; Mattana, M.L.; Rossi, M.; Frimmer, M.; Novotny, L. Quantum control of a nanoparticle optically levitated in cryogenic free space. *Nature* **2021**, *595*, 378–382. [CrossRef] [PubMed]
50. Rossi, M.; Militaru, A.; Zambon, N.C.; Riera-Campeny, A.; Romero-Isart, O.; Frimmer, M.; Novotny, L. Quantum delocalization of a levitated nanoparticle. *Phys. Rev. Lett.* **2025**, *135*, 083601. [CrossRef] [PubMed]
51. Whittle, C.; Hall, E.D.; Dwyer, S.; Mavalvala, N.; Sudhir, V.; Abbott, R.; Ananyeva, A.; Austin, C.; Barsotti, L.; Betzwieser, J.; et al. Approaching the motional ground state of a 10-kg object. *Science* **2021**, *372*, 1333–1336. [CrossRef] [PubMed]

52. Aalbers, J.; AbdusSalam, S.S.; Abe, K.; Aerne, V.; Agostini, F.; Ahmed Maouloud, S.; Akerib, D.S.; Akimov, D.Y.; Akshat, J.; Al Musalhi, A.K.; et al. A next-generation liquid xenon observatory for dark matter and neutrino physics. *J. Phys. G* **2023**, *50*, 013001. [CrossRef]
53. Arnquist, I.J.; Avignone, F.T.; Barabash, A.S.; Barton, C.J.; Bhimani, K.H.; Blalock, E.; Bos, B.; Busch, M.; Buuck, M.; Caldwell, T.S.; et al. Search for spontaneous radiation from wave function collapse in the Majorana Demonstrator. *Phys. Rev. Lett.* **2022**, *129*, 080401. [CrossRef] [PubMed]

Disclaimer/Publisher's Note: The statements, opinions and data contained in all publications are solely those of the individual author(s) and contributor(s) and not of MDPI and/or the editor(s). MDPI and/or the editor(s) disclaim responsibility for any injury to people or property resulting from any ideas, methods, instructions or products referred to in the content.